Developmental Cell
Resource

# A Genomic Multiprocess Survey of Machineries that Control and Link Cell Shape, Microtubule Organization, and Cell-Cycle Progression

Veronika Graml,[1,2,3,6,7] Xenia Studera,[1,2,3,6,8] Jonathan L.D. Lawson,[1,2,6] Anatole Chessel,[1,2,6] Marco Geymonat,[1,2] Miriam Bortfeld-Miller,[3,9] Thomas Walter,[4] Laura Wagstaff,[1,5] Eugenia Piddini,[1,5] and Rafael E. Carazo-Salas[1,2,3,*]
[1]The Gurdon Institute, University of Cambridge, Tennis Court Road, Cambridge CB2 1QN, UK
[2]Genetics Department, University of Cambridge, Downing Street, Cambridge CB2 3EH, UK
[3]Institute of Biochemistry, ETH Zürich, Schafmattstrasse 18, HPM G16.2, Zürich 8093, Switzerland
[4]Institut Curie, Centre for Computational Biology, Centre de Recherche Unité 900, 26 Rue d'Ulm, 75248 Paris Cedex, France
[5]Zoology Department, University of Cambridge, Downing Street, Cambridge CB2 3EJ, UK
[6]Co-first author
[7]Present address: Deloitte Consulting AG, General Guisan-Quai 38, P.O. Box 2232, 8022 Zürich, Switzerland
[8]Present address: PriceSpective, 22 Tudor Street, London EC4Y 0AY, UK
[9]Present address: Institute of Microbiology, ETH Zurich, HCI F 428 Wolfgang-Paulistrasse 10, 8093 Zürich, Switzerland
*Correspondence: cre20@cam.ac.uk
http://dx.doi.org/10.1016/j.devcel.2014.09.005

## SUMMARY

**Understanding cells as integrated systems requires that we systematically decipher how single genes affect multiple biological processes and how processes are functionally linked. Here, we used multiprocess phenotypic profiling, combining high-resolution 3D confocal microscopy and multiparametric image analysis, to simultaneously survey the fission yeast genome with respect to three key cellular processes: cell shape, microtubule organization, and cell-cycle progression. We identify, validate, and functionally annotate 262 genes controlling specific aspects of those processes. Of these, 62% had not been linked to these processes before and 35% are implicated in multiple processes. Importantly, we identify a conserved role for DNA-damage responses in controlling microtubule stability. In addition, we investigate how the processes are functionally linked. We show unexpectedly that disruption of cell-cycle progression does not necessarily affect cell size control and that distinct aspects of cell shape regulate microtubules and vice versa, identifying important systems-level links across these processes.**

## INTRODUCTION

In many ways, the genomes of most organisms remain as black boxes, with the function of the majority of genes and gene products still unknown. This is the case foremost in humans, where, a decade after publication of the human genome sequence, we still have no direct experimental evidence of the function of over half of all the proteins it encodes (http://www.ebi.ac.uk/QuickGO/GAnnotation). Yet this is just the tip of the iceberg because many genes and proteins play roles in multiple biological processes, themselves functionally linked, with most of those multiple roles and links awaiting discovery.

Fission yeast (*Schizosaccharomyces pombe*) is excellently placed for that discovery, with a genome of ~4,900 protein coding genes (26.1% essential), 40% of which have a function only inferred from homology and another 20% completely uncharacterized (Aslett and Wood, 2006; Wood et al., 2002). Over the past four decades, classical genetic screening using *S. pombe* has allowed the discovery of numerous molecules and pathways controlling many essential eukaryotic processes thanks to the genetic tractability, simple morphology, and uniform growth and division pattern of *S. pombe* cells (Forsburg, 2003). Recently, a genome-wide library of knockout (KO) haploid strains—where each of 3,004 nonessential genes across the *S. pombe* genome was systematically deleted—became commercially available (Kim et al., 2010), opening the possibility to potentiate that discovery power using ultrasensitive image-based phenotypic screening strategies (Chia et al., 2012; Collinet et al., 2010; Cotta-Ramusino et al., 2011; Laufer et al., 2013; Mercer et al., 2012; Neumann et al., 2010; Rohn et al., 2011; Simpson et al., 2012; Yin et al., 2013).

Here, we used fission yeast to carry out a 3D image-based genomic screen monitoring cell shape, microtubule organization, and cell-cycle progression to find genes involved in these processes, identify genes controlling multiple processes, and determine how processes are functionally linked. We describe the identification, large-scale validation and quantitative annotation of 262 putative regulators, with 62% newly implicated in the processes studied and 35% implicated in more than one. As a result of in-depth validation of one hit class, we identify a conserved role of the DNA damage response in controlling microtubule stability, revealing a link between those two therapeutically relevant cell biological machineries. Moreover, by exploiting the richness of the multidimensional feature sets obtained from the screen, we investigate statistically and in detail the functional links across processes. We show that disruption of cell-cycle progression does not necessarily affect cell size

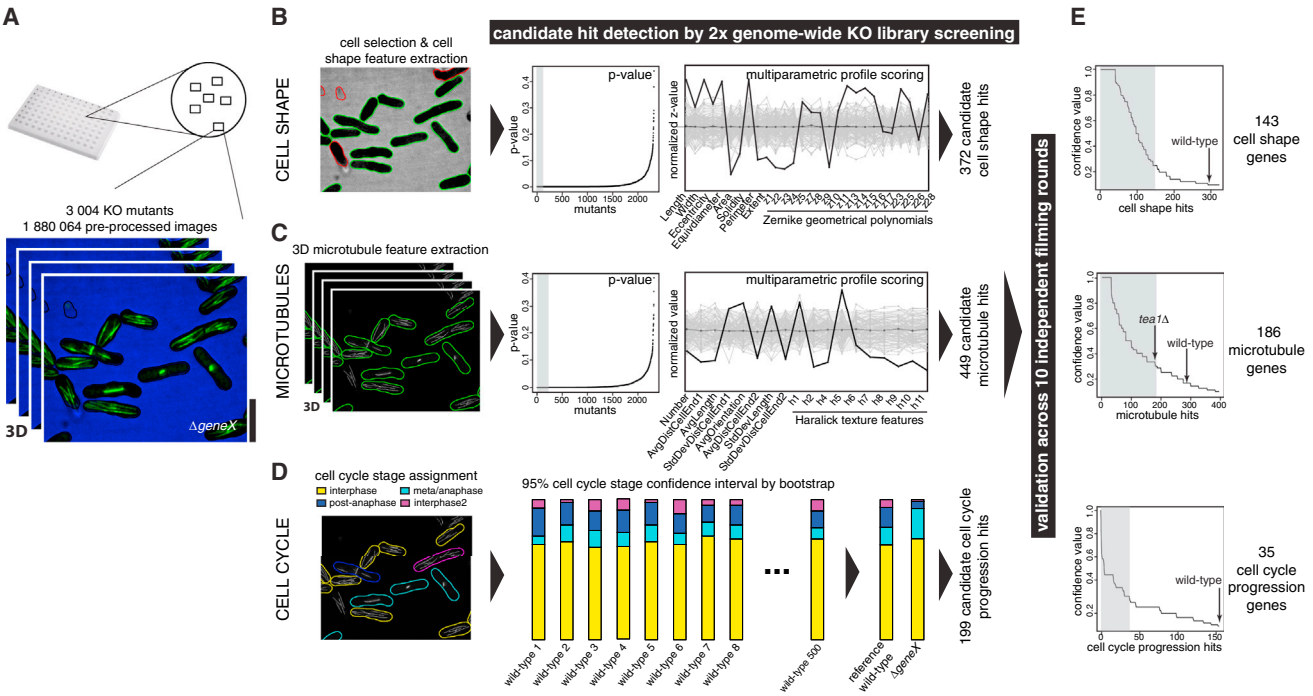


**Figure 1. 3D Image-Based Multiprocess Screening Pipeline and Multiparametric Hit Detection**

(A) A 2× genomic screen input; 3,004 gene KO strains were imaged in 96-well microplates. 3D z stack images were collected from six locations per well in two fluorescence channels to detect cell outlines and GFP-microtubules.

(B and C) Cell shape (B) and microtubule (C) hit detection strategy, using single feature p value measurements to detect extreme hits in one feature (left) or multifeature profile analysis to detect subtle changes across many features (right).

(D) Cell-cycle progression hit identification, by comparison for each mutant of the proportion of its cells assigned to each cell-cycle stage compared to a bootstrapped reference wild-type.

(E) 10-fold high-throughput hit validation using the strategies in (B)–(D). Hits were ranked based on the fraction of independent screening rounds where they were coincidently identified as hits (confidence value). Hits with ≥35% confidence value were subsequently analyzed.

Scale bar represents 10 μm. See also Figures S1–S6 and Tables S1, S2, and S3.

control and that the causal links between cell shape and microtubule regulation in *S. pombe* are directional and complex, with distinct cell shape and microtubule features having defined epistatic relationships in this species.

The multiprocess screen images and gene annotations are available online as a resource for the community at http://www.sysgro.org as well as linked to the centralized fission yeast repository PomBase http://www.pombase.org.

## RESULTS AND DISCUSSION

### Establishment of a 3D Image-Based, Yeast Phenotypic Profiling Pipeline

To carry out a multiprocess phenotypic screen in fission yeast, we developed a live cell, 3D fluorescence image-based phenotypic profiling pipeline combining automated high-resolution spinning disk confocal microscopy and large-scale, quantitative multiparametric image analysis. We used confocal microscopy and 3D (*xyz*) imaging to extract high-resolution subcellular information from individual yeast cells, allowing us to screen with high sensitivity and to obtain refined phenotypic cell biological annotations. Details of the experimental and computational implementation of the pipeline are described in the Experimental Procedures.

We chose to screen for genes controlling cell shape, microtubules, and cell-cycle progression because they are fundamental, well-studied processes for which an extensive, yet likely not exhaustive, list of regulators is known. In addition, all three processes can be monitored simultaneously in live cells expressing only fluorescently labeled tubulin, minimizing manipulation of their genetic background. Indeed, microtubules can be used as bona fide reporters of the cell-cycle state, as they take defined stereotypical patterns across the cell cycle (Hagan, 1998); in turn, cell shape can be simply monitored using extracellular fluorescent dyes (see below). Thus, we generated a version of the genome-wide KO library expressing GFP-tagged endogenous alpha tubulin 2 (GFP-Atb2; Figure 1 and Figure S1A available online), allowing us to visualize microtubules and cell-cycle stage "live" in all mutants. Because the different KO mutants arrayed in 96-well plates had different growth proficiencies compared to the wild-type (Kim et al., 2010), prior to imaging we used a serial dilution and manual repooling strategy to ensure all mutants grew exponentially and were hence physiologically comparable (Figure S1B; Protocol). Then, in preparation for high-throughput imaging, cells were immersed in Cascade blue dextran-containing fluorescent growth medium. This allowed visualization of live cell morphology without the need to express a cytoplasmic fluorophore (Figure 1). Thereafter, mutants in the 96-well plates

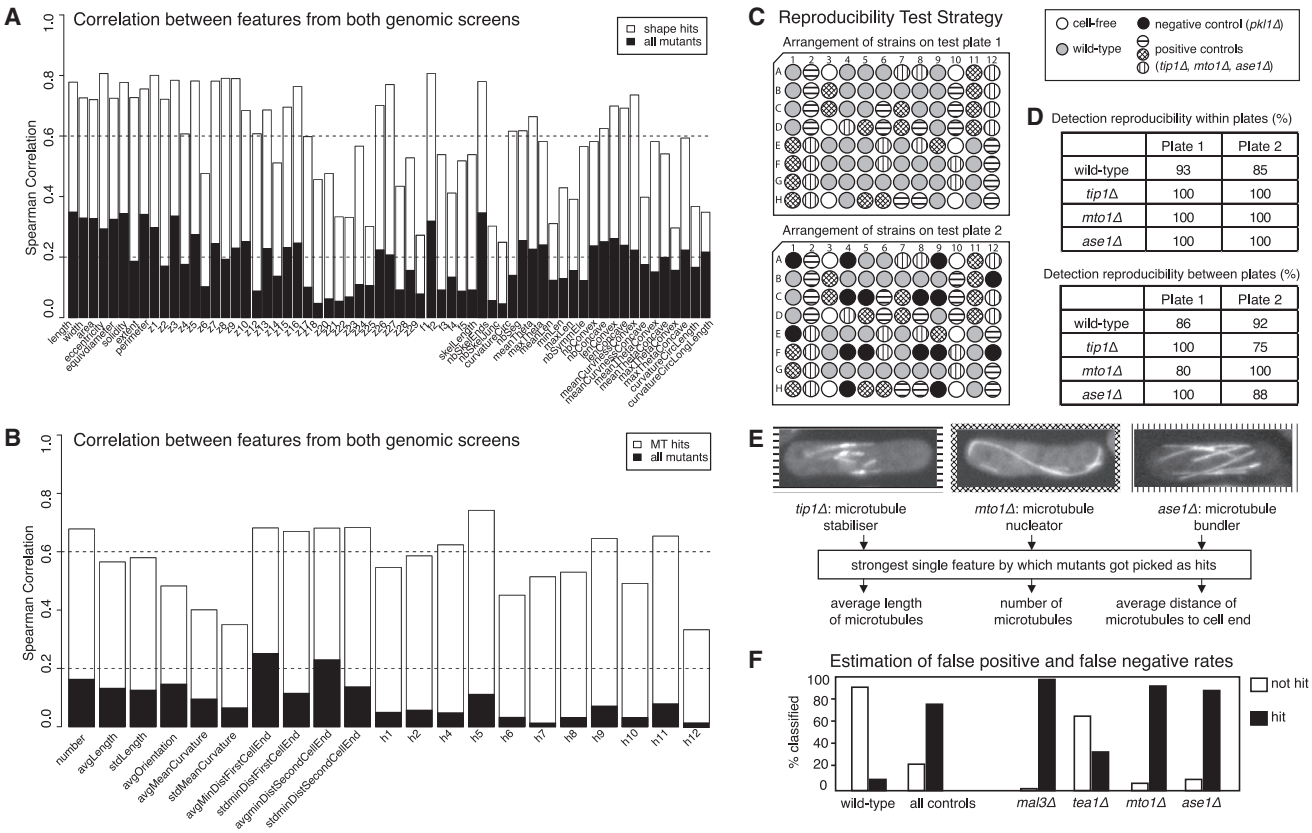


**Figure 2. Quality Control**

(A) Spearman correlation of cell shape features for all mutants and for cell shape hits between the two genomic screening rounds. Only features consistent between both screens were used for analysis.

(B) Similar to (A) for microtubule features.

(C) Arrangement of known microtubule mutants and wild-type cells in plates used in proof-of-method experiments, designed to test for plate location effects and reproducibility of positive and negative control phenotypes.

(D) Percentage of correct identification of mutant versus wild-type populations within and between test plates.

(E) Known mutants used and features for which they were picked.

(F) Rates of incorrect identification of a mutant as wild-type (false-negative rate) for four mutants versus the rate of incorrect identification of wild-type controls as mutant (false-positive rate).

were filmed with two-color (405 nm, 488 nm) automated high-throughput confocal microscopy at high magnification (60× 1.2NA) and in 3D (xy and 16 z planes), and their images computationally analyzed and phenotyped using custom-made image analysis software.

## Quantitative Phenotyping of Cell Shape, Microtubules, and Cell-Cycle Stage

First, we segmented images in the Cascade blue channel, and extracted 57 shape and gray-level features from each 2D cell object (length, width, area, convexity, concavity, topological skeleton, fluorescence intensity along the object's contour, etc.; Figures 1B and 2A; Figure S2 and Table S1). Then, using Machine Learning (Jones et al., 2009; Sommer and Gerlich, 2013), specifically a Random Forest classifier trained with both wild-type shaped and strongly misshapen mutant cells, we identified and rejected poorly segmented objects and kept only well-segmented cells for further analysis (9.28% out-of-bag error rate).

Subsequently, we detected microtubules in the GFP channel xyz image stacks, reconstructed microtubule orientation within every cell in 3D, and extracted 24 geometrical and grey level microtubule features (number, length, fluorescence intensity, orientation, etc.; Figures 1C, 2B, and S3A–S3D; Table S2).

Finally, we identified the cell-cycle stage for each cell based on 3D microtubule pattern, using a four-class support vector machine classifier (Jones et al., 2009; Sommer and Gerlich, 2013),. The classifier, trained with wild-type cells and cells from four known microtubule mutants (lacking Tip1/CLIP170, Brunner and Nurse, 2000; Mto1/Centrosomin, Sawin et al., 2004; Ase1/PRC1, Loïodice et al., 2005; and Pkl1/Kinesin-14A, Troxell et al., 2001) distinguished four cell-cycle-related microtubule patterns: interphase microtubule array (IP; characteristic of G2 phase in our exponential growth conditions), metaphase spindle (SP; characteristic of M phase), postanaphase array (PAA; reflective of G1 phase), and postmitotic interphase microtubule array (called IP2 for "interphase2"; likely reflective of G1-S phases). The classifier accuracy was 93.78% across the wild-type and

four mutants combined, indicating that we could achieve robust cell-cycle stage assignment even when microtubules had an abnormal phenotype. This was partly thanks to the use of 3D microtubule features, which allowed a more accurate assignment of cell-cycle stage than 2D features (see Supplemental Experimental Procedures). The output was a signature of four scores reflecting the proportion of cells assigned to each cell-cycle stage, for each wild-type (typically 70% IP, 10% SP, 10% PAA, and 10% IP2) and mutant cell population, indicative of their cell-cycle progression characteristics (Figures 1D, S3E, and S3F).

### Hit Detection, 10-Fold Validation, and Selection

We used two complementary strategies for detecting KO mutants with aberrant cell shape or microtubules (hits; Figures 1B, 1C, and S4). The first strategy identified mutants with a prominent alteration in a single feature (p value; Figure 1). The second strategy identified mutants with multiple subtle feature alterations (multiparametric profile scoring, Figure 1). In proof-of-principle experiments prior to screening, the use of both strategies combined led to highly consistent detection of the wild-type and of four known microtubule mutants within and across 96-well microplates (Figures 2C–2F), validating the quality and reproducibility of our hit detection strategy. The combined hit detection procedure was optimized independently for cell shape and microtubules based on the results of visual screening by a human observer of one genomic image data set (Figures S5 and S6).

To detect KO mutants (hits) with altered cell-cycle progression, we used bootstrap statistics to estimate the typical proportions of wild-type cells in each cell-cycle stage, scoring as hits KOs where at least two cell-cycle stages were statistically disproportionate with respect to the wild-type (i.e., under- or overrepresented; Figure 1D). That criterion ensured only detection of hits where general cell-cycle progression was affected. In particular, this allowed us to screen for genes distinct from classical cell-cycle regulators which, when mutated, often lead to checkpoint-mediated delay in just one cell-cycle stage or transition.

We grew, imaged, and computationally screened the entire library twice independently (Figures S1C–S1F), analyzing 1,880,064 images and making and analyzing 1,707,870 cell, 5,597,165 microtubule, and 1,607,406 cell-cycle stage assignments. This identified 372 cell shape hits, 449 microtubule hits, and 199 cell-cycle progression hits (note: hit identification for each process was independent of the others). To generate a high-confidence hit list, we then rescreened all hits at large-scale to obtain ten biologically independent screening rounds (also see the Protocol online) and ranked hits according to the fraction of repeats in which they were detected (confidence value; Figure 1E). Only hits with $\geq$35% confidence—the percentage corresponding to a well-established but weak phenotype hit (*tea1Δ*; Figure 2F) added as positive control in all repeats—were selected for further analysis. Altogether, this led to identification of 143 cell shape, 186 microtubules, and 35 cell-cycle progression high-confidence hit genes (Table S3) described next.

### Genes and Pathways Controlling Cell Shape and Cell Size Control

Genes whose KO affected cell shape (cell shape genes; Figure 1E) included expected regulators of cell morphology, cell polarity and growth (Tea3, Pom1, Arf6, Rga2, Tea2, Sla2/End4, Myo1, Efc25, Scd2; for genes' annotations see http://www.pombase.org/) but also many genes related to a wide range of other processes such as trafficking or cell-cycle control, and 17 altogether unannotated genes. Forty-one percent (58/143) of genes implicated in cell shape regulation had not been previously reported as such, to our knowledge. Importantly, they were not identified in a recent visual screen of the *S. pombe* KO library (Hayles et al., 2013). This is likely due to the very different physiological conditions used in that study (nonexponential growth on solid medium) and our use of sensitive computational hit detection.

Similar to previously published studies (Bakal et al., 2007; Fuchs et al., 2010), cell shape hit classification was done using eight support vector machine classifiers trained to recognize eight basic phenotypic classes on an individual cell basis (Figures 3A, 3B, and S4A): stubby (wide), banana (curved), orb (round), kinky (S-shaped), long (elongated), skittle (with one side wider than the other), and T-shaped (branched). Classically, cell shape mutants are thought to display only one aberrant shape phenotype, such as being round or curved (Hayles et al., 2013). Surprisingly we found that, instead, all strains including the wild-type did not display only a single shape phenotype but rather could be defined as a mixture of those eight phenotypes (Figures 3A, 3B, and S4A). Thus, even within a genotypically uniform cell population, the genome allows *S. pombe* cells to explore multiple morphogenetic states. These might be brought about by cell-to-cell differences in the content of key shape-controlling proteins due, for example, to nonexact equipartition of cellular material—polarity landmarks, secretory machinery, cell wall composition/properties, etc.—between daughter cells at cell division or from stochastic gene expression.

Quantitatively, the most common aberrant cell phenotype was stubby (Figure 3C), indicating it may be the most general manifestation of compromised cell shape; conversely the least common was orb (i.e., completely nonpolarized), consistent with the finding that known genes whose disruption leads to complete rounding are essential (Hayles et al., 2013) and with the notion that complete loss of polarity may be incompatible with viability.

We clustered mutants based on their shape phenoprint and found that KOs of specific pathways shared characteristic morphological signatures (Figure 3D). One major cluster of predominantly stubby mutants comprised regulators of endocytosis and exocytosis (Vps25, Vps32, Vps36, Shd1, Dip1, Did4, Sla2/End4, and Sft1; likely involved in apical restriction of cellular growth zones), genes involved in ubiquitin/COP9 signalosome-mediated protein degradation (Csn1, Csn2, Pub1, and Ubi1), and several uncharacterized factors. Another major cluster comprised significantly longer mutants (note: cell elongation, usually associated with cell-cycle deregulation, was scored in our screen as a cell shape defect), corresponding to factors involved in the DNA damage response (DDR; Mre11, Rad50, Rad55, Set1, Ccq1, Cdt2, and Ctp1; the DDR leads to cell-cycle delay and cell elongation), transcriptional regulators (Cuf1 and Rep2), elongator complex subunits (Elp3, Elp4, Elp6, and Dph3; this complex has been involved in negatively regulating exocytosis), histone modifiers (Brl2, Cph1, Cph2, Dep1, and Rtx2), and other putative regulators.

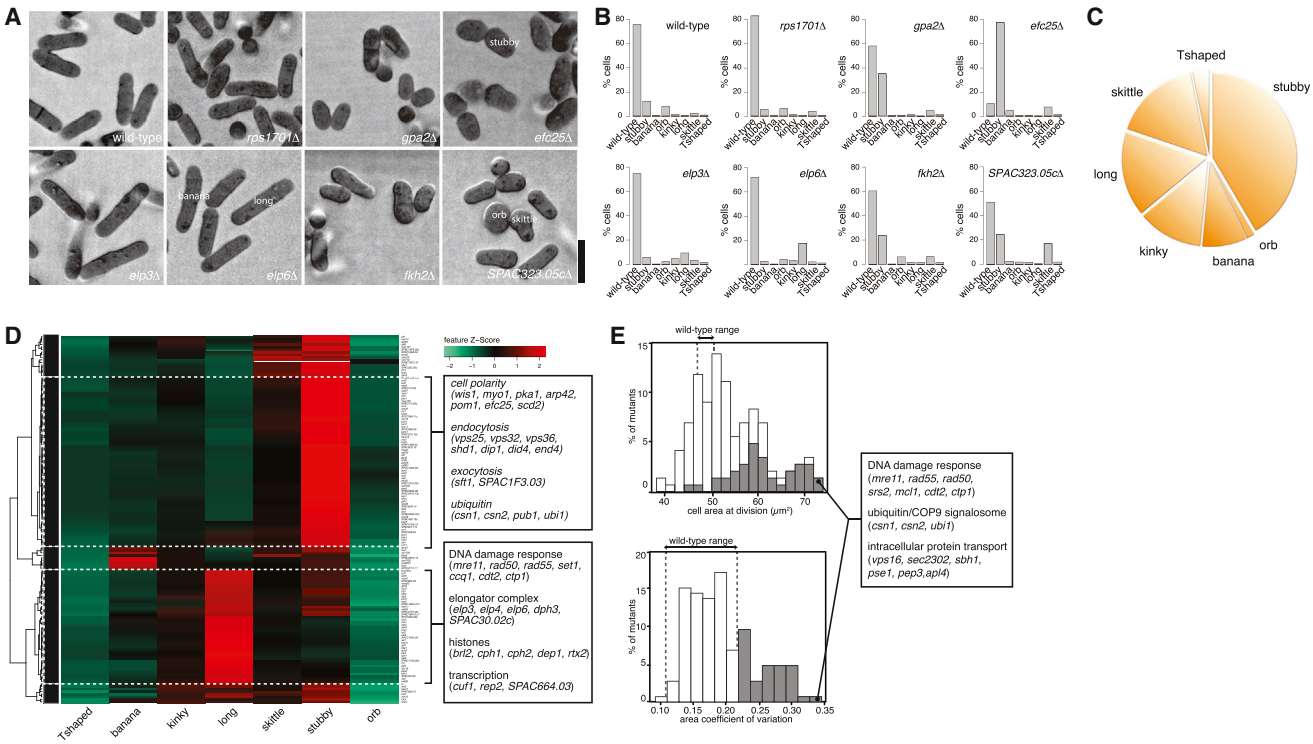


**Figure 3. Cell Shape Genes and Deregulation of Cell Size Control**

(A) Example cell shape hits.

(B) Corresponding cell shape hit shape profiles illustrating the comanifestation of multiple cell shape phenotypes within the genotypically uniform mutant populations.

(C) Phenotypic trait abundance (pie chart) illustrating the proportion of cells from all shape hit populations combined into stereotyped categories.

(D) Phenoprint clustering of cell shape hits based on the shape profiles in (B) and major functional gene ontology (GO) groups.

(E) Distributions of cell size at division (top) and its coefficient of variation (bottom) for cell shape mutants. Mutants with greater coefficient of variation than wild-type are shown in gray with selected gene names.

Scale bar represents 10 μm. See also Figures S2 and S4 and Tables S1 and S3.

We next asked whether, given their geometrical disruption, cell shape mutants properly control cell size. *S. pombe* cells are thought to need to reach a critical cell size at the G1/S and, most importantly, at the G2/M cell-cycle transition, when cells engage in cell division only after reaching twice their original size at birth (Mitchison, 2003). We calculated the average cell area (as a proxy for size) at mitosis by looking at cells containing a mitotic spindle and plotted distributions of the average area at mitosis for all hits (Figure 3E, top) and its coefficient of variation (Figure 3E, bottom). Ninety percent of cell shape hits had an area at division lower or higher than wild-type cells, which divide at an area of ~48 $\mu m^2$. This included KOs of factors known to be involved in cell size control such as Pom1 (Martin and Berthelot-Grosjean, 2009; Moseley et al., 2009). Strikingly, 30% had a higher coefficient of variation of the cell area than the 0.12–0.22 coefficient of the wild-type (gray, Figure 3E), indicative of lack of precision in cell size control at division. Interestingly, the latter was enriched for mutants in the ubiquitin/COP9 signalosome complex (implicated in cell-cycle and cell size control in *Drosophila melanogaster*; Björklund et al., 2006), DDR regulators, and various factors involved in intracellular protein transport. Because the COP9 complex regulates cullin activity in mammals and cullin (Cul-4) has been implicated in both cell-cycle control and the DDR (Hu et al., 2004), one possibility is that ubiquitin/COP9 and the DDR act on cell size control via the same pathway, possibly via their role in cell-cycle regulation. Alternatively, each may play a distinct role that needs to be further explored. Similarly, the role in size control of other factors identified needs to be clarified.

## Genes and Pathways Associated with Characteristic Microtubule Signatures

Genes whose KO affected microtubules (microtubule genes; Figure 1E) included known microtubule regulators (Tea2, Tip1, and Mal3), mitochondrial factors, trafficking-related genes, and 19 altogether unannotated factors. Notably, 93.5% (174/186) of the genes implicated in microtubule regulation had not, to our knowledge, been previously reported as such. Mutants in those genes primarily led to deregulation of microtubule number, length, or orientation, with most KOs affecting several features simultaneously albeit in different proportions (Figure 4A). Microtubule length (encompassing the features: length, length variance, occupancy, occupancy variance; Figures 4B and 4C) was by far the most common quantitatively affected microtubule property, demonstrating that microtubule length per se is not essential for cell viability. In contrast, low microtubule number

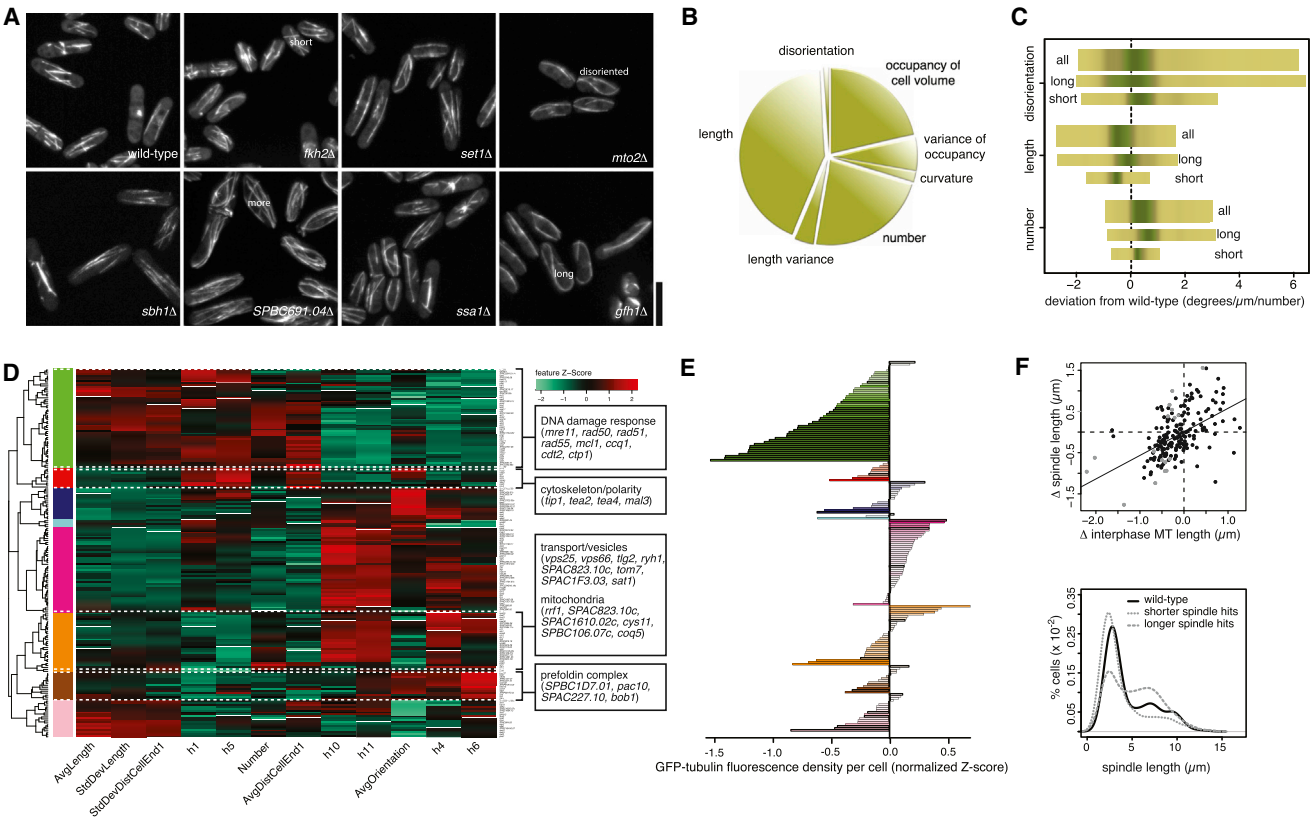


**Figure 4. Genes Associated with Characteristic Microtubule Signatures**

(A) Example microtubule hits.

(B) Phenotypic trait abundance (pie chart) illustrating the proportion of cells from all microtubule mutant cell populations combined displaying a significant phenotype in the features shown.

(C) Three significant features for all (top), only short (bottom) or only long (middle) mutants.

(D) Phenoprint clustering of microtubule hits based on extracted microtubule features and major functional GO groups.

(E) GFP-tubulin content. Average GFP-Atb2 fluorescence level per cell for each mutant is shown in (D) as a proxy for tubulin concentration with respect to the average wild-type value. Colors of the gene groups indicate which clusters from (D) they correspond to.

(F) Correspondence between interphase and mitotic phenotype. Top: comparison of interphase and spindle microtubule length changes for all microtubule hits. Grey: KOs with significantly altered spindle length (spindle hits). Bottom: percentage of cells with a given spindle length, for spindle hits with a spindle shorter/longer than wild-type (shorter/longer spindle hits). In all three classes of populations shown, cells accumulate with a short spindle, likely corresponding to prometaphase state during chromosome capture. Long spindle mutants (gray dashed) also accumulate cells with a longer spindle, which may indicate a delay during or on exiting anaphase B.

Scale bar represents 10 μm. See also Figures S3 and S4 and Tables S2 and S3.

was a very infrequent feature, consistent with the fact that microtubule nucleation is essential for cell viability.

Clustering of microtubule hits was done using a subset of 12 features selected by visual quality control to optimize for high interclass variability and low intraclass variability (i.e., to optimally group together KOs judged visually to have the same phenotype and assign to separate groups KOs with visually different phenotypes) and identified various pathways, each associated with a specific microtubule phenoprint (Figure 4D). Among the most prominent pathways we found were cytoskeleton/cell polarity (Tea2, Tip1, Tea4, Mal3; whose KO leads to short, disoriented microtubules), DDR (Mre11, Rad50, Rad51, Rad55, Mcl1, Ccq1, Cdt2, Ctp1; slightly elongated, hyperoriented microtubules), transport/vesicles and mitochondria (Vps25, Vps66, Tlg2, Ryh1, SPAC823.10c, Tom7, SPAC1F3.03, Sat1, and Rrf1, SPAC823.10c, SPAC1610.02c, Cys11, SPBC106.07c, Coq5; slightly more microtubules), and tubulin folding (the Prefoldin complex subunits SPBC1D7.01, Pac10, SPAC227.10, Bob1; fewer microtubules). We next assessed whether differences in tubulin content could account for the mutants' microtubule feature signatures by quantitating their intracellular GFP-Atb2 fluorescence. We found that, although many mutants displayed substantial differences in tubulin content compared to the wild-type, there was no obvious correlation between their microtubule feature signatures and GFP-tubulin fluorescence, suggesting that their microtubule phenotype arises from deregulation of microtubule assembly rather than tubulin content (Figure 4E). Interestingly, analysis of the hits' microtubule length in interphase versus mitosis revealed a correlation between the two in ~80% of cases (Figure 4F), indicating that many genes identified may also play a role in mitotic spindle control.

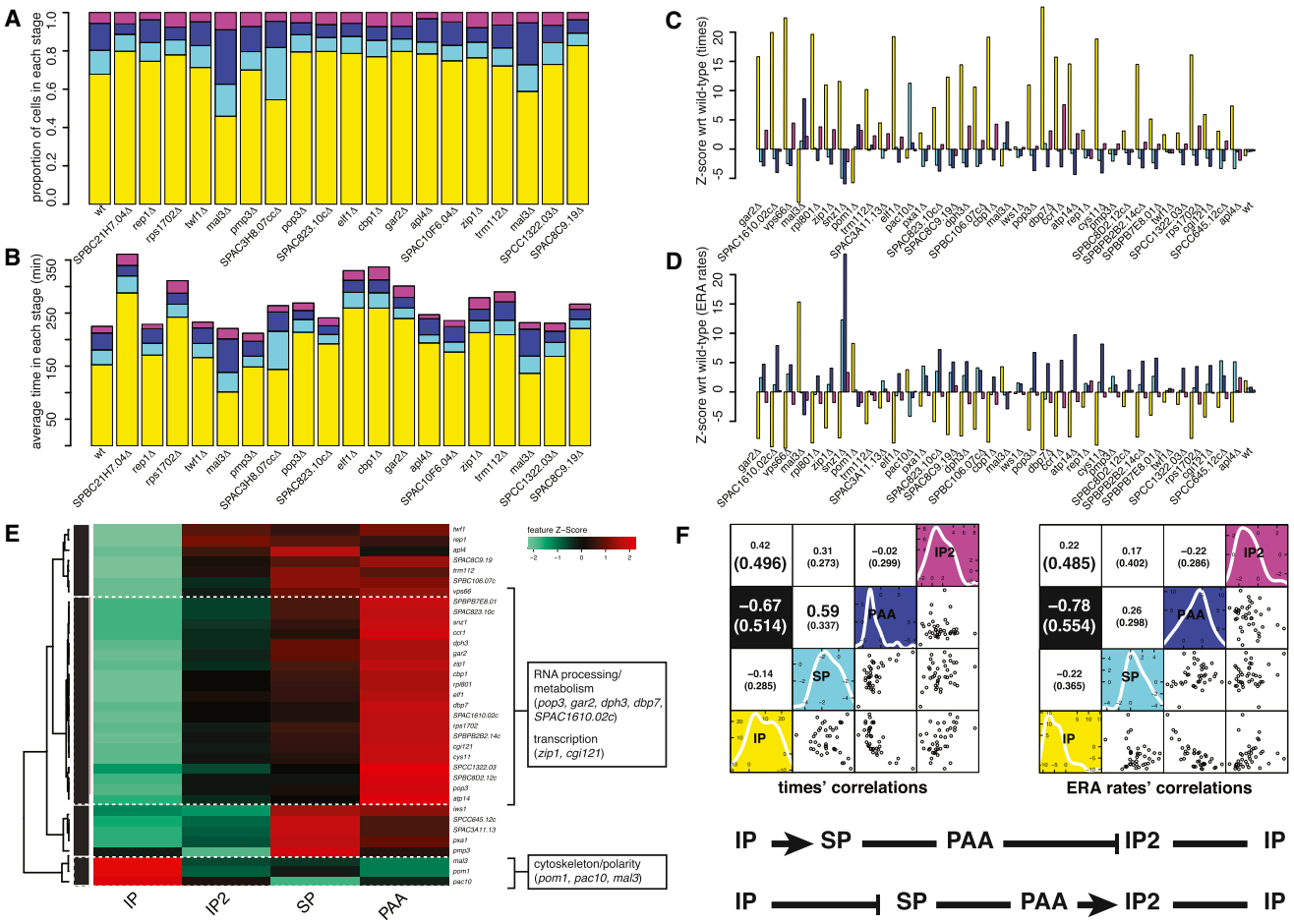


**Figure 5. Cell-Cycle Progression Genes and Cell-Cycle Stage Correlation Analysis**

(A) Proportional representation of the cell-cycle phases—interphase (yellow), spindle (light blue), PAA (blue), interphase 2 (purple)—for a selection of cell-cycle progression hits and a reference wild-type (WT).

(B) As in (A) but with distributions scaled by the doubling time of each mutant.

(C) *Z* score plot showing the significance of deviation from wild-type of cell-cycle stage durations for all hits.

(D) As in (C) for ergodic rate analysis (ERA)-derived progression rates.

(E) Phenoprint clustering based on hits' ERA rates and major functional GO groups.

(F) Correlation analysis among the four cell-cycle stages' durations and ERA progression rates. The graphs show correlation plots of the duration (left graph, bottom half) and rate (right graph, bottom half) of each cell-cycle stage against every other, for all hits. Spearman (and maximal information coefficient, in parentheses) correlation coefficients are shown for each combination in the top half of the graphs. Black boxes indicate significant anticorrelation between the duration and ERA rate of IP and PAA. The diagonal shows the distribution of *Z* score values for the durations (left) and ERA rates (right) across all hits, for each cell-cycle stage quantitated. A diagram representation of the implications of that anticorrelation for the overall cell-cycle is illustrated beneath (pointy arrows: accelerated progression; blunt arrows: delayed progression).

See also Figure S3 and Table S3.

## Cell-Cycle Progression Genes Reveal Temporal Linkage between Nonconsecutive Cell-Cycle Phases

Genes whose KO affected cell-cycle progression (cell-cycle progression genes; Figure 1E) comprised a diverse range of factors and, as expected, did not include classical cell-cycle regulators. To look for interesting functional groups, we measured the cell-cycle duration of all cell-cycle progression hits. This allowed us to convert for each KO the proportions of cells in each cell-cycle stage into average times spent in each stage (Figures 5A and 5B). We then calculated the *Z* score of all four stage times (durations) with respect to the wild-type, for all hits (Figure 5C). Subsequently, we used ergodic rate analysis (ERA; Kafri et al., 2013) to estimate the average rate of progression from each cell-cycle stage to the next (i.e., the rate of exit from each stage) and calculated the ERA rates' *Z* score with respect to the wild-type rates for all cell-cycle progression hits (Figure 5D).

Clustering of the KOs based on their ERA rate *Z* scores (Figure 5E) revealed groups of factors whose KO mainly results in accelerated exit from: IP into SP (Mal3, Pom1, Pac10: cytoskeleton/polarity related), SP into PAA (for example Pxa1: intracellular trafficking; Tos4, Iws1: transcription), PAA into IP2 (the largest group, including Pop3, Gar2, Dph3, Dbp7; RNA processing and metabolism), and IP2 into IP (including Twf1, Apl4: actin and endocytosis). Genes from the first cluster could be involved

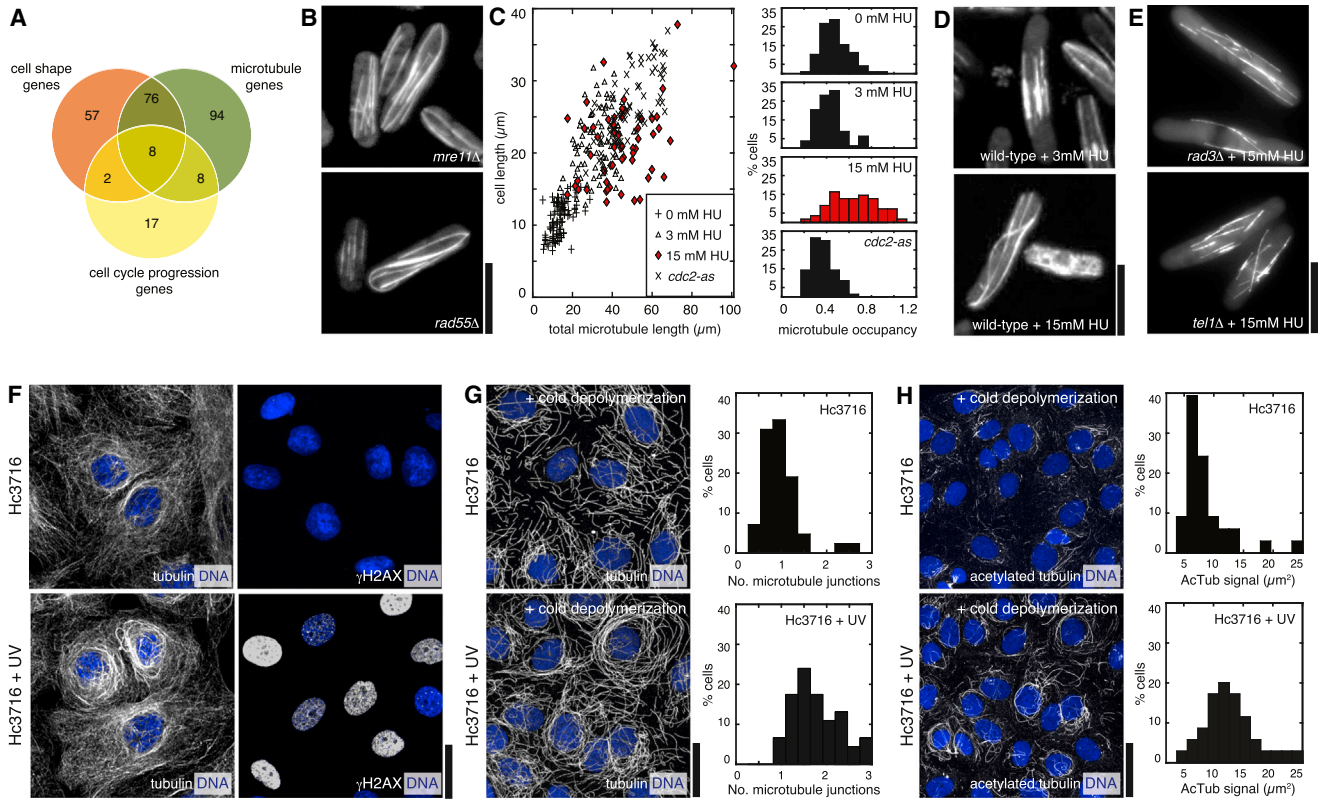


**Figure 6. Genes Regulating Multiple Processes and Role of the DDR in Inducing Interphase Microtubule Stabilization**

(A) Venn diagram illustrating cell shape, microtubule, and cell-cycle progression hits.

(B) The DNA repair defective mutants *mre11Δ* and *rad55Δ* display highly elongated microtubules.

(C) Hydroxyurea (HU) induces disproportionate microtubule elongation in wild-type cells. Microtubule occupancy is the ratio of average microtubule length to cell length. Contrary to 15 mM HU-treated cells, 3 mM HU-treated cells and cell-cycle-arrested *cdc2-as* cells do not disproportionately elongate microtubules.

(D) Images of 3 mM HU- (top) and 15 mM HU-treated cells (bottom).

(E) HU treatment does not induce enhanced microtubule stabilization in the DNA damage checkpoint mutants *rad3Δ* and *tel1Δ*.

(F) Left: effect on microtubules of UV-induced DNA damage in human cultured cells (Hc3716-hTERT). Right: γH2AX staining showing extent of DNA damage.

(G) Contrary to UV-untreated cells, UV-treated cells contain denser (right: quantitations) microtubule bundles that resist cold-induced depolymerization, indicative of microtubule stabilization.

(H) UV-treated cells contain significantly higher acetylated tubulin levels (right: quantitations) than UV-untreated cells.

Scale bars represent 10 μm.

in regulating the IP-SP transition via the Pom1 cell size control pathway (Martin and Berthelot-Grosjean, 2009; Moseley et al., 2009). Some genes from the fourth cluster could control the IP2-IP transition via regulation of the cytokinetic actomyosin ring (Rincon and Paoletti, 2012). It will be interesting to determine how all other genes, known and uncharacterized, are linked to cell-cycle progression control.

Analysis of correlations in durations/rates among the four cell-cycle stages (Spearman or maximal information coefficient; Reshef et al., 2011; Figure 5F) for our hits revealed a strong anticorrelation between IP and PAA, i.e., KOs with an extended IP tend to have a shorter PAA and vice versa. Because IP and PAA reflect G2- and G1-phases, respectively, this suggests that an accelerated G1/S transition (PAA-IP2 exit) causes delayed G2/M transition (IP-SP exit) and vice versa. Because *S. pombe* has been shown to possess two apparently independent cell size control mechanisms acting at G2/M (the dominant one) and G1/S (revealed in small *wee1-50* mutants; Fantes, 1977; Fantes and Nurse, 1978; Mitchison, 2003), which secure that nuclear division does not occur before cells reach a critical size, the observed anticorrelation might reflect compensation in cell-cycle progression caused by one of the mechanisms when the other fails. Interestingly, because the cell-cycle progression mutants identified here did not display altered size at cell division (Figure 6B and next section; contrary for example to *wee1-50* mutants), this suggests that both mechanisms exist and are active even in normally sized cells.

## Genes Involved in Multiple Processes

Of the 262 genes identified for the three processes investigated, 168 (64%) were associated with a single process and 94 (36%) had multiple functional assignments (Figure 6A). Only ten (4%) genes were shared between cell shape and cell-cycle progression and 16 (6%) between microtubules and cell-cycle progression, implying that those processes are largely independent.

In contrast, 84 (32%) genes were shared between cell shape and microtubules, implying a potentially significant coregulation of both processes, as expected. These included factors involved

in cell morphogenesis and polarity (Aah3, Efc25, Tea2, Tip1), endocytosis (Did4, Vps25, Vps36, Snf7), but also transcriptional regulation (Pof3, Pmc6, Rep2, Rxt2, Tup12), chromatin remodeling (Rsc4, Set1, Arp42, Spp1, Swd1), and DDR (Mre11, Rad50, Rad55, Ctp1, Set1, Mcl1, Ubi1). Notably, 60/143 (42%) cell shape genes and 106/186 (57%) microtubule genes had a role in a single process alone. This implies that a link between cell shape and microtubule deregulation is not obligatory in cells and may be specific to particular machineries.

Future work will be needed to clarify which genes the associated with multiple processes actually correspond to factors that actively couple those processes.

## The DDR Induces Stabilization of Interphase Microtubules

The largest functional group of KOs co-deregulating cell shape and microtubules was that of genes related to the DDR. Whereas the role of DDR genes in cell shape control (specifically in cell length and, hence, size control; Figures 3D and 3E) could be understood as resulting from DDR-induced cell-cycle arrest and elongation (Melo and Toczyski, 2002; Zhou and Elledge, 2000), a link between DDR and microtubules (Figure 4D) was unexpected and raised the question of whether DDR gene KOs lead to microtubule deregulation indirectly (via cell shape deregulation) or directly.

Therefore, we decided to investigate this link further and use this as a means to validate the predictions of our phenoprint clustering analysis. Inspection of cells lacking the DNA repair factors Mre11 and Rad55 revealed that in those mutants interphase microtubules are elongated compared to wild-type cells, often curling around cell ends, indicating increased microtubule stability (Figure 6B, quantitation not shown). In contrast, in cells lacking the ATR and ATM checkpoint kinases Rad3 and Tel1 microtubules were of wild-type length (not shown). This suggested that impaired DNA repair functions, and ensuing DDR arising from unrepaired DNA damage, may induce microtubule stabilization via the ATM/ATR pathway. To test this directly, we treated wild-type cells with different doses of hydroxyurea (HU) to induce the DDR in a primarily ATR-dependent manner, and we quantitated the effect of HU dosage on the average length of cellular microtubules and how it scales with cell length (microtubule occupancy). Cells untreated with HU displayed a range of microtubule lengths that varied proportionately with the wild-type range of cell lengths (Figure 6C, 0 mM HU). Similarly, following treatment with a low dose of HU, cells became elongated due to cell-cycle arrest and their microtubules became longer proportionally with cell length increase (Figures 6C and 6D top, 3 mM HU). In contrast, at a higher dose of HU, microtubules became disproportionately longer than cells, indicating an increase in microtubule stability induced specifically by the DDR (Figures 6C and 6D bottom, 15 mM HU). In agreement with this, in elongated G1- and G2-arrested *cdc2-as* mutant cells—where in principle no DDR activation occurs—microtubule elongation was also proportional to cell elongation (Figure 6C quantitations). Furthermore, the enhanced HU-induced microtubule stabilization was specifically DDR dependent, because microtubules did not become stabilized in cells lacking Rad3 or Tel1 treated with 15 mM HU (Figure 6E). Altogether, these data suggest that DNA damage induces microtubule lengthening in an ATR-dependent manner. To test whether this functional link is conserved, we then asked whether induction of DNA damage in human (Hc3716-hTERT) cells by UV treatment (30 J/m$^2$) also elicited a similar effect. We found that in those cells, induction of DDR often causes microtubules to organize in dense bundles around the cell nucleus (Figure 6F and not shown), suggestive of microtubule stabilization. To test this further, we then induced partial microtubule depolymerization by cold (4°C) treatment in both UV-untreated and UV-treated Hc3716 cells. We found that whereas not many UV-untreated cells contain thick bundles after cold depolymerization (1.22%, n = 575 cells; 15% of cell fields scored), many UV-treated cells still contain thick bundles (5.89%, n = 577 cells; 45% of cell fields scored) of much more connected microtubules (Figure 6G). In addition, microtubules in DDR-activated cells contain a much higher amount of acetylated tubulin (Figure 6H), indicative of increased microtubule stability (Hammond et al., 2008). We conclude that the DDR specifically induces stabilization of interphase microtubules, revealing a conserved link between the DDR and cytoskeletal control in cells. Although some links between those two machineries have been reported (Baschal et al., 2006; Lee et al., 2010, 2011; Xie et al., 2011), the conserved link described here points to a more general connection, whose exact physiological role and mechanistic details—in particular the cytoskeletal DDR target(s) involved—will need to be clarified. This might be of particular therapeutic relevance because a combination of cytostatic doses of DNA-damaging drugs with microtubule drugs has been shown to result in selective cytotoxicity and radiation/chemosensitization in some cancer cells (Baumgart et al., 2012; Blagosklonny et al., 2000; Lee et al., 2011).

## Systems-Level Functional Relationships between Processes

One important aspect of our quantitative, multiprocess screening strategy is that it allowed us, beyond hit identification and phenotypic clustering, to obtain rich multidimensional feature sets characterizing all three processes simultaneously in cells, for hundreds of different KO conditions. Hence, we exploited the richness of those multidimensional feature sets to investigate statistically the systems-level functional relationships across processes.

We first turned to cell-cycle progression hits—selected as having at least two disproportionate cell-cycle stages with respect to the wild-type (Figure 1D)—and asked whether their cell-cycle progression defect quantitatively affected their cell size. Remarkably, we found that their cell size distribution—as assessed by measuring cells undergoing division—was indistinguishable from that of wild-type cells (Figure 7A). This is in contrast with mutants in conventional cell-cycle genes, which have traditionally been identified by virtue of their abnormal cell size phenotype, and indicates that the cell-cycle progression genes uncovered here likely constitute a mechanistically distinct class of cell-cycle regulators. Likewise and importantly, it demonstrates that disruption of cell-cycle progression does not necessarily affect cell size control.

We next turned to cell shape and microtubule hits and investigated dependencies between their features using Bayesian network analysis (Collinet et al., 2010; Yu et al., 2004). Like correlation analysis, Bayesian network analysis allows graphical

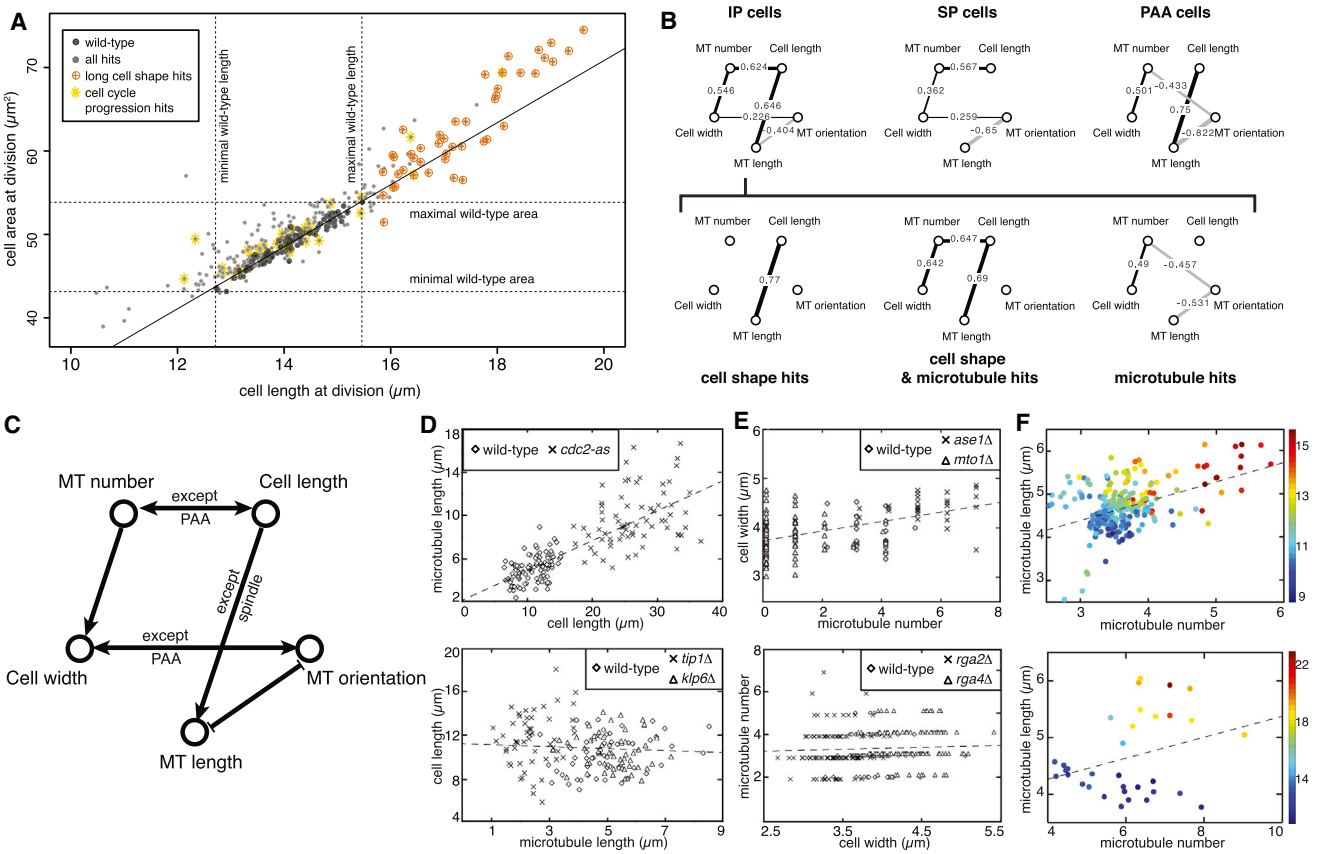


**Figure 7. Systems-Level Functional Interactions between Processes**

(A) Distribution of cell length and area at division for long cell shape hits (orange) versus cell-cycle progression hits (yellow). Note their lack of intersection. Wild-type controls (black) and other hits (gray) are shown, for comparison.

(B) Bayesian network inference graphs of the conditional correlation between cell shape and microtubule features across hits, filtered by cell-cycle stage (top row) or, for interphase cells only, subdivided by hitlist (cell shape and/or microtubule; bottom row). Correlation coefficients between variables are displayed on top of network edges (note that correlations were not directly used to obtain the networks).

(C) Diagram summarizing significant Bayesian causal links between cell shape and microtubule regulation in *S. pombe*.

(D) Causation between cell length and microtubule length. Top: plot of interphase cell length and microtubule length for wild-type and *cdc2-as* cells. Bottom: the inverse plot for cells with shorter (*tip1Δ*) or longer (*klp6Δ*) microtubules. Note that cell length influences specifically microtubule length, not the inverse.

(E) Causation between microtubule number and cell width. Top: plot of microtubule number against cell width for cells with more (*ase1Δ*) and fewer (*mto1Δ*) microtubules. Bottom: inverse plot for wider (*rga4Δ*) and narrower (*rga2Δ*) cells. To aid visualization, points have been artificially displaced along the microtubule number axis for different genotypes. Note that microtubule number influences specifically cell width, not the inverse.

(F) Plots of microtubule number against microtubule length colored by cell length (different colors signify different cell lengths), illustrating that correlation between these features is dependent upon cell length. Top: data from genomic screens; each point represents the average of all cells analyzed for a given mutant. Bottom: low-throughput validation using cells artificially elongated by cell-cycle arrest.

See also Figure S7.

representation of the probabilistic relationships between variables in a data set. However, in addition Bayesian networks allow inferring conditional dependencies between variables. Thus, two variables are disconnected in a Bayesian network graph if they are either independent or conditionally independent knowing one or several other variables. This allows inference of direct links between two variables, as opposed to indirect effects mediated or caused by a third variable.

We focused on five key features quantitated in our screen: microtubule number, microtubule length, microtubule (dis)orientation, cell length, and cell width. Using data from all cell shape and microtubule hits together, we constructed three Bayesian networks corresponding to three different cell-cycle stages (IP, SP, and PAA) by using for each network only cells in the corresponding cell-cycle stage, and compared edges between the networks. We found that, whereas specific pairs of features are interdependent in a consistently correlated or anticorrelated manner, many of those dependencies are cell-cycle stage-specific (Figure 7B, top three graphs; +, correlation; −, anticorrelation; Figure S7 illustrates the robustness of the analysis). For example, we found that cell length and microtubule number are always linked in cells except during postanaphase (PAA), when a profuse, radial microtubule network assembles in the cell middle. Similarly, cell width and microtubule (dis)orientation are always linked except in postanaphase, indicating that in this species not only interphase microtubule alignment but also

mitotic spindle orientation relies mostly on cellular geometry (Théry et al., 2007). Instead, cell length and microtubule length are interdependent except during mitosis, indicating that mitotic spindle size is independent of cell size in this species (Wilbur and Heald, 2013).

We then constructed three different Bayesian networks using features from KOs deregulated in cell shape, microtubules or both (Figure 7B, bottom three graphs), and visually compared the networks to seek to infer directionality in the dependencies among features. We found that cell length and microtubule length are linked in hits deregulated in cell shape alone and in hits deregulated in both cell shape and microtubules. Instead, the two features are not linked in hits deregulated in microtubules only. We interpret this as implying that the causality is from cell length to microtubule length (e.g., increased cell length promotes increased microtubule length). Conversely and unexpectedly, we found that microtubule number and cell width are linked in microtubule-only hits and in cell shape and microtubule hits, but not in hits only deregulated in cell shape, leading us to interpret that the causality in this case is from microtubule number to cell width (e.g., increased microtubule number in cells promotes increased cell width). These results are summarized in Figure 7C.

To corroborate the inferred statistical relationships, we sought to externally validate some of its predictions. First, we looked at *cdc2-as* cells—which have altered cell length due to cell-cycle arrest—and found (Figure 6C) that, in this mutant, cell length changes induce proportional microtubule length changes (Figure 7D, top). In contrast, in mutants lacking the microtubule stabilizer Tip1/CLIP170 or the catastrophe-promoting kinesin-like protein Klp6/Kinesin-8—with, respectively, shorter and longer microtubules—microtubule length changes do not induce cell length changes (Figure 7D, bottom). Thus, cell length controls microtubule length and not the reverse, as predicted.

Second, we looked at mutants lacking the microtubule bundling protein Ase1/PRC1 or the microtubule nucleation factor Mto1/Centrosomin—with, respectively, a higher and lower number of microtubule bundles—and found that in those mutants, microtubule number changes induce cell width changes (Figure 7E, top). Instead and in contrast, in mutants lacking the Rho2 GTPase-activating protein Rga2 or the Cdc42/Rho2 GTPase-activating protein Rga4—narrower and wider than wild-type cells, respectively—cell width changes do not induce microtubule number changes (Figure 7E, bottom). Hence, microtubule number controls cell width and not the reverse, as inferred.

Third, we asked whether, as implied by the analysis, microtubule number and microtubule length are not directly linked. The absence of that direct link is interesting (despite the fact that microtubule number and length are known to be regulated by different machineries in cells) because one could expect both features to be somewhat dependent on one another, given that both rely on the common pool of tubulin available in each cell. In fact, plotting microtubule length versus number—both using the screen data set (Figure 7F, top) and external data from wild-type, 3mM HU-treated and *cdc2-as* cells for validation (Figure 7F, bottom)—showed a positive correlation between both features, implying a link between them. However, the correlation was absent among cells of similar length (Figure 7F). This demonstrates that, as predicted, microtubule number is not directly linked to microtubule length but rather both features are conditionally independent knowing cell length, i.e., they are coupled indirectly via the length of the cell.

Thus, the causal relationship between cell shape and microtubule regulation in *S. pombe* is directional and complex, with specific cell shape and microtubule features having defined epistatic relationships. Importantly, although our preliminary validation from Figures 7D–7F suggests that Bayesian analysis is indeed a useful predictor, given the partial and therefore potentially misleading nature of the parametrical description we have used, it will be crucial in the future to carefully validate the other predictions obtained using this approach.

## Conclusions

In an effort to begin deciphering systematically how genes affect multiple cell biological processes and how processes are functionally linked, we carried out a quantitative multiprocess screen simultaneously monitoring three fundamental cell biological processes: cell shape, microtubule organization, and cell-cycle progression.

Our screen identified and annotated 262 genes, 131 of which were uncharacterized in *S. pombe* (of those, 29 had no predicted function in any species) and 131 had been described in the context of a different process, including six genes of the ubiquitin/elongator pathways not implicated in cell shape control; 39 membrane trafficking/mitochondrial genes, which we show are involved in microtubule regulation; and nine RNA processing/metabolism genes implicated in cell-cycle progression. We also probed in depth the systemic relationships among those three processes—identifying 94 genes regulating multiple processes and functional relationships linking defined aspects of such processes, in particular cell shape and microtubule control. This provides a rich, quantitative genomic data set available for further mining, validation, and mechanistic analysis by the scientific community (available at http://www.sysgro.org and http://www.pombase.org).

We extrapolate that an important gain in unexpected mechanistic insights could be obtained from multiprocess screening across an increasing range of cell biological processes, using simple unicellular systems with standardized/optimized genomic KO or siRNA/RNAi libraries (Collinet et al., 2010). A future challenge therefore lies in developing graphical and statistical modeling approaches (Nicolau et al., 2011; Singh et al., 2007) suited to cope with the very high dimensionality information generated by such screens, in particular to combine information from independent studies (Kemmer et al., 2009; Nicolau et al., 2011; Spalding et al., 2000; Troyanskaya et al., 2003) in a representable and interpretable manner. Such developments will be key to obtain a systemic picture of cell function and to better understand and predict synergistic or antagonistic interactions, including those among clinically relevant compounds (Horn et al., 2011).

## EXPERIMENTAL PROCEDURES

Full methods are available in the Supplemental Experimental Procedures; specific standards for the synchronization and rescreening of thousands of parallel yeast strains are included in the Protocol.

### Knockout Screen for Cell Shape, Microtubule, and Cell-Cycle Progression Genes

The Bioneer haploid deletion (knockout, KO) library v.2 (Bioneer, Korea) was modified to generate a GFP-tubulin expressing library (Dixon et al., 2008). KO mutants were grown exponentially for >48 hr and imaged in 96-well microplates (lectin-coated glass bottom, 10 μg/well) containing Cascade Blue Dextran-labeled YES medium (0.1 mg/ml). Two-color images were acquired using an automated OperaLX spinning-disk confocal microscope (Perkin Elmer) with 60× water-immersion objective (NA 1.2). Six stacks of 16 z planes 0.4 μm separation were collected for each well. The entire genomic KO library was filmed twice. Customized software was used for image analysis and feature extraction.

### Hit Detection, Large-Scale Validation, and Bayesian Analysis

Cell shape or microtubule hits were KO strains with a: (1) low Kolmogorov-Smirnov p value relative to a mean wild-type for any one feature, or (2) significant Euclidean distance deviation from a mean wild-type across many features. Cell-cycle progression hits were KOs with the proportion of cells in greater than two 2-cell cycle stages outside the 95% bootstrap confidence interval of the corresponding wild-type stages. Genotypic and visual quality controls were done for corroboration. Hits were large-scale validated with ten times independent rescreening (see Protocol) and if picked in ≥35% of cases kept as high-confidence hits for analysis. Support vector machine classifiers assigned eight phenotypic classes to cell shape hits. ERA rates (Kafri et al., 2013) were calculated for cell-cycle progression hits. Clustering used R, functional GO assignments DAVID, Bayesian analysis, and the R package bnlearn (Scutari, 2010).

### Investigation of DNA Damage Response and Microtubules

Yeasts were treated with HU 9 hr before filming and every 3 hr afterward and were imaged on lectin-coated MatTek dishes using a DeltaVision system (GE Healthcare). Hc3716-hTERT cells were grown to 70% confluence in Hepatocyte Medium Bullet Kit, exposed to 30 J/m$^2$ UVC, and grown for 8 hr before cold treatment or fixing. Immunostaining for β-tubulin or α-acetylated tubulin was done with ALEXAfluor-conjugated secondary antibodies, and DNA was DAPI-labeled. Cells were imaged with a Leica SP5 confocal microscope.

## SUPPLEMENTAL INFORMATION

Supplemental Information includes Supplemental Experimental Procedures, seven figures, three tables, and one protocol and can be found with this article online at http://dx.doi.org/10.1016/j.devcel.2014.09.005.

## AUTHOR CONTRIBUTIONS

R.E.C.-S. conceived/led the project and designed the general experimental and computational strategy. X.S. and M.B.M carried out preliminary experiments and generated the modified *S. pombe* haploid deletion library used. X.S. and J.L. carried out all experimental yeast work and imaging with continuous help from M.G. V.G. developed the image processing and large-scale analysis tools for screening and clustering with continuous help from A.C. A.C. carried out all Bayesian network inference work and ERA computation and correlation. T.W. contributed expertise in image analysis and data mining. R.E.C.-S. and E.P. designed the mammalian cell UV treatment experiments, and E.P. and L.W. carried out all mammalian cell work. R.E.C.-S. wrote the text with help from other coauthors.

## ACKNOWLEDGMENTS

We thank Y. Barral, M. Peter, C. Wilson-Zbinden, D. Gerlich, G. Székely, P. Horvath, M. Held, D. Brunner, T. Makushok, J. Ellenberg, P. Nurse, J. Hayles, A. Sossick, C. Bradshaw, N. Samusik, S. Tooze, A. Csikász-Nagy, F. Vaggi, M. Sato, C. Schmidt, S. Jackson, J. Ahringer, D. St Johnston, V. Wood, P. Zegerman, E. Khabirova, C. Stocker, J. Pines, and the Carazo-Salas group for help and comments; A. Sossick and N. Lawrence for assistance with imaging; S. Jackson for antibodies (gamma-H2AX) and use of the UVC box; M. Sato for *S. pombe* strains; and J. Pines, S. Jackson, P. Horvath, F. Navarro, and E. Miska for critical reading of the manuscript. This work was supported by a European Research Council Starting Researcher Investigator grant (to R.E.C.-S.; SYSGRO), a SystemsX.ch Interdisciplinary PhD grant (to R.E.C.-S.; 2009-026), a Swiss National Foundation Project Grant (to R.E.C.-S.; 3100A0_120656/1), a Human Frontier Science Program Young Investigator grant (to R.E.C.-S. and A.C.; HFSP RGY0066/2009-C), a Biological Sciences Research Council Responsive Mode grant (to R.E.C.-S.; BB/K006320/1), an Isaac Newton Trust research grant (to R.E.C.-S.; 10.44(n)), a Wellcome Trust PhD studentship (to J.L.D.L.), a University Research Fellowship from the Royal Society (to E.P.; UF0905080), and a Cancer Research UK Programme Grant (to E.P.; A12460).

Received: November 2, 2013
Revised: April 21, 2014
Accepted: August 19, 2014
Published: October 27, 2014

## REFERENCES

Aslett, M., and Wood, V. (2006). Gene Ontology annotation status of the fission yeast genome: preliminary coverage approaches 100%. Yeast *23*, 913–919.

Bakal, C., Aach, J., Church, G., and Perrimon, N. (2007). Quantitative morphological signatures define local signaling networks regulating cell morphology. Science *316*, 1753–1756.

Baschal, E.E., Chen, K.J., Elliott, L.G., Herring, M.J., Verde, S.C., and Wolkow, T.D. (2006). The fission yeast DNA structure checkpoint protein Rad26ATRIP/LCD1/UVSD accumulates in the cytoplasm following microtubule destabilization. BMC Cell Biol. *7*, 32.

Baumgart, T., Klautke, G., Kriesen, S., Kuznetsov, S.A., Weiss, D.G., Fietkau, R., Hildebrandt, G., and Manda, K. (2012). Radiosensitizing effect of epothilone B on human epithelial cancer cells. Strahlentherapie und Onkologie. Organ der Deutschen Rontgengesellschaft *188*, 177–184.

Björklund, M., Taipale, M., Varjosalo, M., Saharinen, J., Lahdenperä, J., and Taipale, J. (2006). Identification of pathways regulating cell size and cell-cycle progression by RNAi. Nature *439*, 1009–1013.

Blagosklonny, M.V., Robey, R., Bates, S., and Fojo, T. (2000). Pretreatment with DNA-damaging agents permits selective killing of checkpoint-deficient cells by microtubule-active drugs. J. Clin. Invest. *105*, 533–539.

Brunner, D., and Nurse, P. (2000). CLIP170-like tip1p spatially organizes microtubular dynamics in fission yeast. Cell *102*, 695–704.

Chia, J., Goh, G., Racine, V., Ng, S., Kumar, P., and Bard, F. (2012). RNAi screening reveals a large signaling network controlling the Golgi apparatus in human cells. Mol. Syst. Biol. *8*, 629.

Collinet, C., Stöter, M., Bradshaw, C.R., Samusik, N., Rink, J.C., Kenski, D., Habermann, B., Buchholz, F., Henschel, R., Mueller, M.S., et al. (2010). Systems survey of endocytosis by multiparametric image analysis. Nature *464*, 243–249.

Cotta-Ramusino, C., McDonald, E.R., 3rd, Hurov, K., Sowa, M.E., Harper, J.W., and Elledge, S.J. (2011). A DNA damage response screen identifies RHINO, a 9-1-1 and TopBP1 interacting protein required for ATR signaling. Science *332*, 1313–1317.

Dixon, S.J., Fedyshyn, Y., Koh, J.L., Prasad, T.S., Chahwan, C., Chua, G., Toufighi, K., Baryshnikova, A., Hayles, J., Hoe, K.L., et al. (2008). Significant conservation of synthetic lethal genetic interaction networks between distantly related eukaryotes. Proc. Natl. Acad. Sci. USA *105*, 16653–16658.

Fantes, P.A. (1977). Control of cell size and cycle time in Schizosaccharomyces pombe. J. Cell Sci. *24*, 51–67.

Fantes, P.A., and Nurse, P. (1978). Control of the timing of cell division in fission yeast. Cell size mutants reveal a second control pathway. Exp. Cell Res. *115*, 317–329.

Forsburg, S.L. (2003). Overview of Schizosaccharomyces pombe. Current Protocols in Molecular Biology *64*, 13.14.1–13.14.3.

Fuchs, F., Pau, G., Kranz, D., Sklyar, O., Budjan, C., Steinbrink, S., Horn, T., Pedal, A., Huber, W., and Boutros, M. (2010). Clustering phenotype populations by genome-wide RNAi and multiparametric imaging. Mol. Syst. Biol. *6*, 370.

Hagan, I.M. (1998). The fission yeast microtubule cytoskeleton. J. Cell Sci. *111*, 1603–1612.

Hammond, J.W., Cai, D., and Verhey, K.J. (2008). Tubulin modifications and their cellular functions. Curr. Opin. Cell Biol. *20*, 71–76.

Hayles, J., Wood, V., Jeffery, L., Hoe, K.L., Kim, D.U., Park, H.O., Salas-Pino, S., Heichinger, C., and Nurse, P. (2013). A genome-wide resource of cell cycle and cell shape genes of fission yeast. Open biology *3*, 130053.

Horn, T., Sandmann, T., Fischer, B., Axelsson, E., Huber, W., and Boutros, M. (2011). Mapping of signaling networks through synthetic genetic interaction analysis by RNAi. Nat. Methods *8*, 341–346.

Hu, J., McCall, C.M., Ohta, T., and Xiong, Y. (2004). Targeted ubiquitination of CDT1 by the DDB1-CUL4A-ROC1 ligase in response to DNA damage. Nat. Cell Biol. *6*, 1003–1009.

Jones, T.R., Carpenter, A.E., Lamprecht, M.R., Moffat, J., Silver, S.J., Grenier, J.K., Castoreno, A.B., Eggert, U.S., Root, D.E., Golland, P., and Sabatini, D.M. (2009). Scoring diverse cellular morphologies in image-based screens with iterative feedback and machine learning. Proc. Natl. Acad. Sci. USA *106*, 1826–1831.

Kafri, R., Levy, J., Ginzberg, M.B., Oh, S., Lahav, G., and Kirschner, M.W. (2013). Dynamics extracted from fixed cells reveal feedback linking cell growth to cell cycle. Nature *494*, 480–483.

Kemmer, D., McHardy, L.M., Hoon, S., Rebérioux, D., Giaever, G., Nislow, C., Roskelley, C.D., and Roberge, M. (2009). Combining chemical genomics screens in yeast to reveal spectrum of effects of chemical inhibition of sphingolipid biosynthesis. BMC Microbiol. *9*, 9.

Kim, D.U., Hayles, J., Kim, D., Wood, V., Park, H.O., Won, M., Yoo, H.S., Duhig, T., Nam, M., Palmer, G., et al. (2010). Analysis of a genome-wide set of gene deletions in the fission yeast Schizosaccharomyces pombe. Nat. Biotechnol. *28*, 617–623.

Laufer, C., Fischer, B., Billmann, M., Huber, W., and Boutros, M. (2013). Mapping genetic interactions in human cancer cells with RNAi and multiparametric phenotyping. Nat. Methods *10*, 427–431.

Lee, H., Jeon, J., Ryu, Y.S., Jeong, J.E., Shin, S., Zhang, T., Kang, S.W., Hong, J.H., and Hur, G.M. (2010). Disruption of microtubules sensitizes the DNA damage-induced apoptosis through inhibiting nuclear factor κB (NF-κB) DNA-binding activity. J. Korean Med. Sci. *25*, 1574–1581.

Lee, K.J., Lin, Y.F., Chou, H.Y., Yajima, H., Fattah, K.R., Lee, S.C., and Chen, B.P. (2011). Involvement of DNA-dependent protein kinase in normal cell cycle progression through mitosis. J. Biol. Chem. *286*, 12796–12802.

Loïodice, I., Staub, J., Setty, T.G., Nguyen, N.P., Paoletti, A., and Tran, P.T. (2005). Ase1p organizes antiparallel microtubule arrays during interphase and mitosis in fission yeast. Mol. Biol. Cell *16*, 1756–1768.

Martin, S.G., and Berthelot-Grosjean, M. (2009). Polar gradients of the DYRK-family kinase Pom1 couple cell length with the cell cycle. Nature *459*, 852–856.

Melo, J., and Toczyski, D. (2002). A unified view of the DNA-damage checkpoint. Curr. Opin. Cell Biol. *14*, 237–245.

Mercer, J., Snijder, B., Sacher, R., Burkard, C., Bleck, C.K., Stahlberg, H., Pelkmans, L., and Helenius, A. (2012). RNAi screening reveals proteasome- and Cullin3-dependent stages in vaccinia virus infection. Cell Reports *2*, 1036–1047.

Mitchison, J.M. (2003). Growth during the cell cycle. Int. Rev. Cytol. *226*, 165–258.

Moseley, J.B., Mayeux, A., Paoletti, A., and Nurse, P. (2009). A spatial gradient coordinates cell size and mitotic entry in fission yeast. Nature *459*, 857–860.

Neumann, B., Walter, T., Hériché, J.K., Bulkescher, J., Erfle, H., Conrad, C., Rogers, P., Poser, I., Held, M., Liebel, U., et al. (2010). Phenotypic profiling of the human genome by time-lapse microscopy reveals cell division genes. Nature *464*, 721–727.

Nicolau, M., Levine, A.J., and Carlsson, G. (2011). Topology based data analysis identifies a subgroup of breast cancers with a unique mutational profile and excellent survival. Proc. Natl. Acad. Sci. USA *108*, 7265–7270.

Reshef, D.N., Reshef, Y.A., Finucane, H.K., Grossman, S.R., McVean, G., Turnbaugh, P.J., Lander, E.S., Mitzenmacher, M., and Sabeti, P.C. (2011). Detecting novel associations in large data sets. Science *334*, 1518–1524.

Rincon, S.A., and Paoletti, A. (2012). Mid1/anillin and the spatial regulation of cytokinesis in fission yeast. Cytoskeleton (Hoboken) *69*, 764–777.

Rohn, J.L., Sims, D., Liu, T., Fedorova, M., Schöck, F., Dopie, J., Vartiainen, M.K., Kiger, A.A., Perrimon, N., and Baum, B. (2011). Comparative RNAi screening identifies a conserved core metazoan actinome by phenotype. J. Cell Biol. *194*, 789–805.

Sawin, K.E., Lourenco, P.C., and Snaith, H.A. (2004). Microtubule nucleation at non-spindle pole body microtubule-organizing centers requires fission yeast centrosomin-related protein mod20p. Current biology: CB *14*, 763–775.

Scutari, M. (2010). Learning Bayesian Networks with the bnlearn R Package. J. Stat. Softw. *35*, 1–22.

Simpson, J.C., Joggerst, B., Laketa, V., Verissimo, F., Cetin, C., Erfle, H., Bexiga, M.G., Singan, V.R., Hériché, J.K., Neumann, B., et al. (2012). Genome-wide RNAi screening identifies human proteins with a regulatory function in the early secretory pathway. Nat. Cell Biol. *14*, 764–774.

Singh, G., Mémoli, F., and Carlsson, G.E. (2007). Topological methods for the analysis of high dimensional data sets and 3d object recognition. Eurographics Symposium on Point-Based Graphics *22*, 91–100.

Sommer, C., and Gerlich, D.W. (2013). Machine learning in cell biology - teaching computers to recognize phenotypes. J. Cell Sci. *126*, 5529–5539.

Spalding, D.J.M., Harker, A.J., and Bayliss, M.K. (2000). Combining high-throughput pharmacokinetic screens at the hits-to-leads stage of drug discovery. Drug Discov. Today *5* (12, Suppl 1), 70–76.

Théry, M., Jiménez-Dalmaroni, A., Racine, V., Bornens, M., and Jülicher, F. (2007). Experimental and theoretical study of mitotic spindle orientation. Nature *447*, 493–496.

Troxell, C.L., Sweezy, M.A., West, R.R., Reed, K.D., Carson, B.D., Pidoux, A.L., Cande, W.Z., and McIntosh, J.R. (2001). pkl1(+)and klp2(+): Two kinesins of the Kar3 subfamily in fission yeast perform different functions in both mitosis and meiosis. Mol. Biol. Cell *12*, 3476–3488.

Troyanskaya, O.G., Dolinski, K., Owen, A.B., Altman, R.B., and Botstein, D. (2003). A Bayesian framework for combining heterogeneous data sources for gene function prediction (in Saccharomyces cerevisiae). Proc. Natl. Acad. Sci. USA *100*, 8348–8353.

Wilbur, J.D., and Heald, R. (2013). Mitotic spindle scaling during Xenopus development by kif2a and importin α. eLife *2*, e00290.

Wood, V., Gwilliam, R., Rajandream, M.A., Lyne, M., Lyne, R., Stewart, A., Sgouros, J., Peat, N., Hayles, J., Baker, S., et al. (2002). The genome sequence of Schizosaccharomyces pombe. Nature *415*, 871–880.

Xie, P., Li, L., Xing, G., Tian, C., Yin, Y., He, F., and Zhang, L. (2011). ATM-mediated NuSAP phosphorylation induces mitotic arrest. Biochem. Biophys. Res. Commun. *404*, 413–418.

Yin, Z., Sadok, A., Sailem, H., McCarthy, A., Xia, X., Li, F., Garcia, M.A., Evans, L., Barr, A.R., Perrimon, N., et al. (2013). A screen for morphological complexity identifies regulators of switch-like transitions between discrete cell shapes. Nat. Cell Biol. *15*, 860–871.

Yu, J., Smith, V.A., Wang, P.P., Hartemink, A.J., and Jarvis, E.D. (2004). Advances to Bayesian network inference for generating causal networks from observational biological data. Bioinformatics *20*, 3594–3603.

Zhou, B.B., and Elledge, S.J. (2000). The DNA damage response: putting checkpoints in perspective. Nature *408*, 433–439.